ELSEVIER

Journal of Fluids and Structures 19 (2004) 785–800

JOURNAL OF
FLUIDS AND
STRUCTURES

www.elsevier.nl/locate/jnlabr/yjfls

Computation of the aeroelastic response of a flexible delta wing at high angles of attack

R.E. Gordnier*, M.R. Visbal

Air Force Research Laboratory, AFRL/VAAC, Building 146 Room 225, 2210 Eighth Street, Wright-Patterson AFB, OH 45433-7512, USA

Received 7 October 2003; accepted 15 April 2004

Abstract

To perform relevant aeroelastic analyses for a delta wing at an angle of attack, a computational technique capable of addressing both complex nonlinear aerodynamics and nonlinear structural features is presented. This numerical method couples a well-validated Euler/Navier–Stokes code (Euler computations only in present work) with a nonlinear finite-element plate model. The resulting aeroelastic solver is used to simulate a 60° sweep flexible delta wing for angles of attack from 5° to 40°. When vortex breakdown is present over the wing, increased buffeting of the wing is observed consistent with previous experimental observations. Comparisons of the computed r.m.s. wingtip acceleration with experimentally measured values shows good qualitative agreement. Spectral analysis of the wingtip deflection and acceleration show the first structural mode to be the dominant mode with participation also from the second and third mode.

Published by Elsevier Ltd.

Keywords: Delta wing; Buffet; von Karman plate model; Vortex breakdown

---

1. Introduction

The new unmanned combat air vehicle (UCAV) configurations being developed will need to be highly maneuverable while allowing for increased flexibility in the wing structure. These vehicles often incorporate delta-type wing shapes of more moderate sweep (40°–60°). While extensive investigations of highly swept (> 60°), rigid delta wings have been made both experimentally and computationally, significantly less research has been undertaken for these higher aspect-ratio delta wing configurations. Furthermore, very few researchers have examined the interaction of the resulting unsteady vortical flow with a flexible delta wing. Further research is required to provide a better understanding of the aeroelastic response of a delta wing at angle of attack.

Previous computational investigations of the aeroelastic response of delta wings have focused on the occurrence of limit-cycle oscillations (LCO) at small ($<2°$) angle of attack. Tang and Dowell (Tang et al., 1999; Tang and Dowell, 2001) coupled a vortex lattice aerodynamic model with the von Karman plate equations to determine the theoretical flutter boundary beyond which LCO occurs for delta wings with sweep angles of 30°, 45° and 60°. Tang and Dowell (Tang et al., 2001, 2002) also explored the nonlinear aeroelastic response of a delta wing to periodic gusts. One of the present authors (Gordnier, 2002) has also simulated the limit cycle response of a cropped delta wing with a 47.8° leading-edge sweep. For these computations a well-validated Navier–Stokes solver was coupled with a finite element

---

*Corresponding author. Tel.: +1-937-904-4051; fax: +1-937-656-7867.

E-mail addresses: raymond.gordnier@wpafb.af.mil (R.E. Gordnier), miguel.visbal@wpafb.af.mil (M.R. Visbal).

0889-9746/$ - see front matter Published by Elsevier Ltd.
doi:10.1016/j.jfluidstructs.2004.04.008

Nomenclature

A_{ij}	membrane rigidities
c	root chord length
Cp	pressure coefficient
D	plate stiffness, $E_s\bar{h}^3/12(1-\nu^2)$
D_{ij}	flexural rigidities
$\tilde{D}^{ij}$	structural damping submatrices
E_s	Young's modulus
E	total specific energy
$\hat{F}, \hat{G}, \hat{H}$	inviscid vector fluxes
h	nondimensional plate thickness, $\bar{h}/c$
$\bar{h}$	plate thickness
J	transformation Jacobian
M_∞	freestream Mach number
M_{xx}, M_{yy}, M_{xy}	bending and twisting moments
M^{11}, M^{22}, M^{33}	mass submatrices
N_{xx}, N_{yy}, N_{xy}	membrane stresses
p	pressure
St	Strouhal number, $\mathrm{St} = fc/u_\infty$
t	nondimensional time $t = \bar{t}u_\infty/c$
u, v, w	velocity components in x, y and z
x, y, z	physical coordinates
$\delta u, \delta v, \delta w$	midplane surface displacements
α	angle of attack
β	Newmark's β constant, $\beta = 0.25$
$\varepsilon_{xx}, \varepsilon_{yy}, \gamma_{xy}$	von Karman strains
λ	dynamic pressure, $\rho_\infty u_\infty^2 c^3/D$
μ	viscosity coefficient
μ_s	mass ratio, $\rho_\infty c/\rho_s\bar{h}$
ξ, η, ζ	computational coordinates
ρ	density
ρ_s	structural mass density
$\phi_j(x, y)$	Hermite interpolation functions
$\psi_j(x, y)$	Lagrange interpolation functions
$(\dot{\cdot})$	time differentiation

model for the von Karman plate equations. For the very small angles of attack considered in the above works, the development of a leading-edge vortex system over the delta wing does not play a significant role.

As the angle of attack of a delta wing is increased, however, a pair of leading-edge vortices form. At higher incidence, these vortices undergo a process called vortex breakdown or vortex burst, which leads to the development of a highly unsteady flow over the delta wing. The phenomenon of vortex breakdown has been extensively studied, and reviews of the vortex breakdown problem over delta wings have been given by Visbal (1995a) and Rockwell (1993). Other sources of unsteady vortex flow behavior include Kelvin–Helmholtz shear layer instabilities (Gordnier and Visbal, 1994), fluctuations of vortex breakdown location (Gursul and Xie, 1999) and vortex shedding at very high angles of attack (Gursul and Xie, 1999). These different unsteady vortex regimes result in a range of relevant characteristic time scales for this problem that vary by several orders of magnitude (Menke et al., 1996).

The coherent fluctuations associated with vortex breakdown can result in unsteady responses from aircraft structures. The most common example of this is the 'tail buffet' phenomena which arises from the interaction of the vortex breakdown flow with the vertical tail structure. Much less studied, however, is how a delta wing itself responds to this type of unsteady flow behavior. Recently, Gray et al. (2003) have performed an experiment to investigate the aeroelastic response of a 60° sweep flat plate delta wing to this type of coherent fluctuations. They found an increase in the root mean square (r.m.s.) buffeting response with the onset of vortex breakdown over the wing. The maximum buffeting occurred when vortex breakdown was close to the apex of the wing. Once full wing stall was achieved, a rapid drop in the buffeting response was observed. The present paper investigates computationally this same delta wing configuration and the numerical results are compared with these experimental measurements.

While the complex, vortical flows described above require higher-fidelity models to simulate the delta-wing aerodynamics, the proper modelling of the structural response of the delta wing also presents a challenge. Recent work by Tang et al. (1999) and Gordnier (2002) demonstrated the importance of geometric nonlinearities in capturing the correct structural response of a delta wing. Furthermore, future UCAV configurations may employ new types of composite materials which will introduce their own nonlinear structural behavior. Structural models capable of treating these kinds of nonlinear structural features will be required.

Given the above simulation challenges, to perform relevant aeroelastic analyses for a delta wing at an angle of attack, a computational technique capable of addressing both complex, nonlinear aerodynamics and nonlinear structural features is required. The present author has developed such a technique (Gordnier and Fithen, 2001; Gordnier, 2002) which couples a well-validated Navier–Stokes or Euler solver with a nonlinear, finite-element plate model. Subiterations are used to synchronize the aerodynamic and structural solvers. In the present work, the Euler solver will be used to simulate the primary vortical flow features of interest for the sharp-edged delta wing.

2. Aerodynamics solver

2.1. Governing equations

The equations chosen to model the aerodynamics are the unsteady, compressible, three-dimensional Euler equations written in nondimensional, strong-conservation law form (Pulliam and Steger, 1980) employing a general time-dependent transformation. The resulting system of governing equations is expressed as

$$\frac{\partial \hat{U}}{\partial t}+\frac{\partial \hat{F}}{\partial \xi}+\frac{\partial \hat{G}}{\partial \eta}+\frac{\partial \hat{H}}{\partial \zeta}=0. \tag{1}$$

With this formulation, the vector of dependent variables $\hat{U}$ is given as

$$\hat{U}=\frac{1}{J}U=\frac{1}{J}[\rho \;\; \rho u \;\; \rho v \;\; \rho w \;\; \rho E]^{\mathrm{T}}. \tag{2}$$

All variables have been normalized by the appropriate combination of freestream density, velocity and a characteristic length. The perfect gas relationship closes the system of equations. For the sharp-edged delta wing simulated in the present work, the Euler equations adequately model the primary vortical flow features resulting from the separation of the flow from the sharp leading edge. At high angles of attack the breakdown of the primary vortex is also captured with this set of equations.

2.2. Finite difference procedure

Solutions of Eq. (1) are obtained numerically using the implicit approximately factored finite-difference algorithm of Beam and Warming (1978), employing a Newton-like subiteration procedure (Gordnier and Visbal, 1991). Second-order temporal accuracy is secured in this iterative approach by selecting $\phi=\frac{1}{2}$ in Eq. (3). The numerical algorithm is written in approximately factored, delta form as

$$\begin{aligned}&\left[J^{-1^{p+1}}+\phi^{i}\Delta t_{s}\delta_{\xi}\left(\frac{\partial \hat{F}^{p}}{\partial U}\right)\right]J^{p+1}\left[J^{-1^{p+1}}+\phi^{i}\Delta t_{s}\delta_{\eta}\left(\frac{\partial \hat{G}^{p}}{\partial U}\right)\right]J^{p+1}\left[J^{-1^{p+1}}+\phi^{i}\Delta t_{s}\delta_{\zeta}\left(\frac{\partial \hat{H}^{p}}{\partial U}\right)\right]\Delta U\\&\quad=-\phi^{i}\Delta t_{s}\left[J^{-1^{p+1}}\frac{(1+\phi)U^{p}-(1+2\phi)U^{n}+\phi U^{n-1}}{\Delta t}-U^{p}\left(\left(\frac{\xi_t}{J}\right)_{\xi}+\left(\frac{\eta_t}{J}\right)_{\eta}+\left(\frac{\zeta_t}{J}\right)_{\zeta}\right)^{p+1}+\delta_{\xi}(\hat{F}^{p})+\delta_{\eta}(\hat{G}^{p})+\delta_{\zeta}(\hat{H}^{p})\right],\end{aligned} \tag{3}$$

where

$$\phi^{i}=\frac{1}{1+\phi}, \qquad \Delta U=U^{p+1}-U^{p}; \tag{4}$$

for $p=1$, $U^{p}=U^{n}$ and as $p\rightarrow\infty$, $U^{p}\rightarrow U^{n+1}$.

With this subiteration approach the right-hand side of Eq. (3) represents the numerical approximation to the governing equation, while the left-hand side vanishes as $p\rightarrow\infty$. The left-hand side, therefore, may be modified without loss of formal accuracy provided a sufficient number of subiterates is employed. In particular, diagonalizing the left-hand side of Eq. (3) following the approach of Pulliam and Chaussee (1981) improves the efficiency of the algorithm. Although the diagonalized form of the ADI scheme is only first-order time-accurate, when coupled with subiterations, higher-order time accuracy may be recovered (Morton et al., 1997). Furthermore, a time step on the left-hand side of the equation Δt_s, may be chosen independently from the physical time step Δt on the right-hand side, thereby enhancing stability. The right-hand side of Eq. (3) may also be modified to include a higher-order, upwind-biased algorithm [Roe scheme of Gaitonde et al. (1995)] and lagged boundary conditions without destroying the implicit nature of the method.

In Eq. (3) all spatial derivatives are approximated by second-order accurate central differences, and common forms of both implicit and explicit nonlinear dissipation (Jameson et al., 1981) are employed in order to preserve numerical stability. The temporal metric derivatives are discretized in a manner consistent with the temporal derivative of the conserved variables in Eq. (3).

When solving fluid/structure interactions, the aerodynamic mesh must be allowed to move in accordance with the motion of the structural surface. A simple algebraic method described in Melville et al. (1997) deforms the aerodynamic mesh to accommodate the changing surface position. This grid motion strategy has proved adequate for the wing motions considered in the present work. In order to ensure satisfaction of the geometric conservation law (GCL) for the moving mesh, the identity

$$\frac{\partial J^{-1}}{\partial t} + \left(\frac{\xi_t}{J}\right)_\xi + \left(\frac{\eta_t}{J}\right)_\eta + \left(\frac{\zeta_t}{J}\right)_\zeta = 0 \tag{5}$$

has been used to evaluate the term $(\partial J^{-1}/\partial t)$ in Eq. (3).

3. Structural dynamics solver

3.1. Governing equations

The governing structural equations are the von Karman equations which are required for large plate deflections. Derivations for these equations may be found in a number of sources, including Chia (1980). For this theory the plate is assumed to be of uniform small thickness. The normal deflection of the plate is assumed to be on the order of the thickness of the plate, while the tangential displacements are assumed infinitesimal. Kirchoff's hypothesis is employed with tractions on surfaces parallel to the middle surface assumed negligible and strains varying linearly with the plate thickness. As a result of these assumptions, the displacements $(\delta u^*, \delta v^*, \delta w^*)$ at any point in the plate become

$$\left\{\begin{array}{c}\delta u^*(x,y,z,t)\\ \delta v^*(x,y,z,t)\\ \delta w^*(x,y,z,t)\end{array}\right\} = \left\{\begin{array}{c}\delta u(x,y,t) + \dfrac{z}{h}\dfrac{\partial \delta w}{\partial x}\\ \delta v(x,y,t) + \dfrac{z}{h}\dfrac{\partial \delta w}{\partial y}\\ \delta w(x,y,t)\end{array}\right\}, \tag{6}$$

where $\delta u, \delta v, \delta w$ are the displacements on the midplane of the plate. Using these expressions the von Karman strains have the following form:

$$\left\{\begin{array}{c}\varepsilon_{xx}\\ \varepsilon_{yy}\\ \gamma_{xy}\end{array}\right\} = \left\{\begin{array}{c}\varepsilon^0_{xx}\\ \varepsilon^0_{yy}\\ \gamma^0_{xy}\end{array}\right\} + z\left\{\begin{array}{c}\varepsilon^1_{xx}\\ \varepsilon^1_{yy}\\ \gamma^1_{xy}\end{array}\right\}, \tag{7}$$

where

$$\left\{\begin{array}{c}\varepsilon^0_{xx}\\ \varepsilon^0_{yy}\\ \gamma^0_{xy}\end{array}\right\} = h^2\left\{\begin{array}{c}\dfrac{\partial \delta u}{\partial x} + \dfrac{1}{2}\left(\dfrac{\partial \delta w}{\partial x}\right)^2\\ \dfrac{\partial \delta v}{\partial y} + \dfrac{1}{2}\left(\dfrac{\partial \delta w}{\partial y}\right)^2\\ \dfrac{\partial \delta u}{\partial y} + \dfrac{\partial \delta v}{\partial x} + \dfrac{\partial \delta w}{\partial x}\dfrac{\partial \delta w}{\partial y}\end{array}\right\} \tag{8}$$

and

$$\begin{Bmatrix} \varepsilon^1_{xx} \\ \varepsilon^1_{yy} \\ \gamma^1_{xy} \end{Bmatrix} = -h \begin{Bmatrix} \dfrac{\partial^2 \delta w}{\partial x^2} \\ \dfrac{\partial^2 \delta w}{\partial y^2} \\ 2\dfrac{\partial^2 \delta w}{\partial x \partial y} \end{Bmatrix}. \tag{9}$$

With these relations the governing equations for the plate motion are written as

$$\begin{aligned} &\frac{\lambda}{\mu_s}\frac{\partial^2 \delta w}{\partial t^2} - \frac{\partial^2}{\partial x^2}\left(\frac{\lambda}{h} M_{xx}\right) - 2.0\frac{\partial^2}{\partial x \partial y}\left(\frac{\lambda}{h} M_{xy}\right) - \frac{\partial^2}{\partial y^2}\left(\frac{\lambda}{h} M_{yy}\right) \\ &\quad - \frac{\partial}{\partial x}\left(\lambda N_{xx}\frac{\partial \delta w}{\partial x} + \lambda N_{xy}\frac{\partial \delta w}{\partial y}\right) - \frac{\partial}{\partial y}\left(\lambda N_{xy}\frac{\partial \delta w}{\partial x} + \lambda N_{yy}\frac{\partial \delta w}{\partial y}\right) = \frac{\lambda}{h} q, \end{aligned} \tag{10}$$

$$h^2 \frac{\lambda}{\mu_s}\frac{\partial^2 \delta u}{\partial t^2} - \frac{\partial \lambda N_{xx}}{\partial x} - \frac{\partial \lambda N_{xy}}{\partial y} = 0, \tag{11}$$

$$h^2 \frac{\lambda}{\mu_s}\frac{\partial^2 \delta v}{\partial t^2} - \frac{\partial \lambda N_{xy}}{\partial x} - \frac{\partial \lambda N_{yy}}{\partial y} = 0, \tag{12}$$

where

$$\begin{Bmatrix} M_{xx} \\ M_{yy} \\ M_{xy} \end{Bmatrix} = \begin{bmatrix} D_{11} & D_{12} & 0 \\ D_{21} & D_{22} & 0 \\ 0 & 0 & D_{66} \end{bmatrix} \begin{Bmatrix} \varepsilon^1_{xx} \\ \varepsilon^1_{yy} \\ \gamma^1_{xy} \end{Bmatrix}, \tag{13}$$

$$\begin{Bmatrix} N_{xx} \\ N_{yy} \\ N_{xy} \end{Bmatrix} = \begin{bmatrix} A_{11} & A_{12} & 0 \\ A_{21} & A_{22} & 0 \\ 0 & 0 & A_{66} \end{bmatrix} \begin{Bmatrix} \varepsilon^0_{xx} \\ \varepsilon^0_{yy} \\ \gamma^0_{xy} \end{Bmatrix}. \tag{14}$$

These equations are cast in a Lagrangian reference frame where x, y and z refer to the original undeflected plate location. The equations have been nondimensionalized based on the freestream density, freestream velocity and the length of the plate. In addition, the nondimensional displacements δu and δv have been scaled by the square of the nondimensional plate thickness, h^2. Similarly, δw has been scaled by the nondimensional plate thickness, h. In these equations $\lambda = 12(1 - \nu^2)\rho_\infty u_\infty^2 c^3 / E_s \bar{h}^3$ is the nondimensional freestream dynamic pressure and $\mu_s = \rho_\infty c / \rho_s \bar{h}$ is the mass ratio. The terms A_{ij} and D_{ij} are referred to as the membrane and flexural rigidities, respectively. For an isotropic plate the values of these terms are given by $A_{11} = A_{22} = 12/\lambda h^2, A_{12} = A_{21} = \nu A_{11}, A_{66} = (1 - \nu)A_{11}/2, D_{11} = D_{22} = 1/\lambda, D_{12} = D_{21} = \nu D_{11}, D_{66} = (1 - \nu)D_{11}/2$, where ν is Poisson's ratio.

Eqs. (10)–(12) are a coupled set of nonlinear equations for the plate deflections. The nonlinear terms in Eq. (10) arise due to the stretching of the middle surface of the plate resulting in the development of the membrane stresses N_{xx}, N_{yy}, and N_{xy}. The linear plate equations are recovered by assuming the membrane stresses to be negligible.

3.2. Finite element model

The finite element model developed for the plate Eqs. (10)–(12) is based on a 4 node, conforming, rectangular plate element described in Reddy (1993). The nodal degrees of freedom are $\delta u, \delta v, \delta w, \partial \delta w/\partial x, \partial \delta w/\partial y$, and $\partial^2 \delta w/\partial x \partial y$. The deflections δu and δv are interpolated using Lagrange interpolation functions $\delta u = \sum_{j=1}^4 \delta u_j \psi_j(x, y)$ and $\delta v = \sum_{j=1}^4 \delta v_j \psi_j(x, y)$. The deflection δw is interpolated using Hermite interpolation functions $\delta w = \sum_{j=1}^{16} \Delta_j \phi_j(x, y)$ where Δ_j consists of the values of $\delta w, \partial \delta w/\partial x, \partial \delta w/\partial y$, and $\partial^2 \delta w/\partial x \partial y$ at the four nodes.

To derive the finite element model, Eqs. (10)–(12) are rewritten in their weak form. The expressions for $\delta u, \delta v$, and δw are then substituted giving the following set of finite element equations:

$$\begin{bmatrix} [M^{11}] & [0] & [0] \\ [0] & [M^{22}] & [0] \\ [0] & [0] & [M^{33}] \end{bmatrix} \begin{Bmatrix} \{\delta\ddot{u}\} \\ \{\delta\ddot{v}\} \\ \{\delta\ddot{W}\} \end{Bmatrix}^{p+1} + \begin{bmatrix} [\tilde{D}^{11}] & [\tilde{D}^{12}] & [\tilde{D}^{13}] \\ [\tilde{D}^{21}] & [\tilde{D}^{22}] & [\tilde{D}^{23}] \\ [\tilde{D}^{31}] & [\tilde{D}^{32}] & [\tilde{D}^{33}] \end{bmatrix} \begin{Bmatrix} \{\delta\dot{u}\} \\ \{\delta\dot{v}\} \\ \{\delta\dot{W}\} \end{Bmatrix}^{p+1}$$

$$+ \begin{bmatrix} [K^{11}] & [K^{12}] & [K^{13}] \\ [K^{21}] & [K^{22}] & [K^{23}] \\ [K^{31}] & [K^{32}] & [K^{33}] \end{bmatrix} \begin{Bmatrix} \{\delta u\} \\ \{\delta v\} \\ \{\delta W\} \end{Bmatrix}^{p+1} = \begin{Bmatrix} \{F^1\} \\ \{F^2\} \\ \{F^3\} \end{Bmatrix}, \tag{15}$$

where

$$\delta W = \left[\delta w \quad \frac{\partial \delta w}{\partial x} \quad \frac{\partial \delta w}{\partial y} \quad \frac{\partial^2 \delta w}{\partial x \partial y} \right]^{\mathrm{T}}. \tag{16}$$

Expressions for the matrices $[M^{ij}], [\tilde{D}^{ij}]$, and $[K^{ij}]$ may be found in Gordnier (2002). The nonlinear terms in Eqs. (10)–(12) have been linearized about the previous subiteration level p. As in the aerodynamic solver, subiterations are used to minimize the error introduced by this linearization. Evaluation of the integrals is accomplished by a Hermite interpolation of the element coordinates to a master element where Gaussian quadrature is performed.

The time integration of Eq. (15) is accomplished using Newmark's β method (Humar, 1990). In Newmark's β method, the displacements, δu, δv, δw and velocities, $\delta\dot{u}$, $\delta\dot{v}$, $\delta\dot{w}$ are computed using the following relations (here shown for δw):

$$\delta\dot{w}^{p+1} = \delta\dot{w}^n + \frac{\Delta t}{2}(\delta\ddot{w}^n + \delta\ddot{w}^{p+1}), \tag{17}$$

$$\delta w^{p+1} = \delta w^n + \Delta t \delta\dot{w}^n + \tfrac{1}{2}(1 - 2\beta)\Delta t^2 \delta\ddot{w}^n + \beta \Delta t^2 \delta\ddot{w}^{p+1}. \tag{18}$$

In the present work the value $\beta = \frac{1}{4}$ is always used. For this value of β, the scheme reduces to the average acceleration method where the acceleration over an interval is held constant at a value equal to the average of the acceleration at the beginning and end of the interval. This method is second order accurate in time and unconditionally stable.

4. Aerodynamic/structural coupling

Coupling of the aerodynamics with the structural response occurs through the aerodynamic forces, q, in Eqs. (10)–(12) and by the resulting deflection of the plate, δw, which is returned to the aerodynamic grid. Implicit coupling of these two sets of equations is achieved by replacing the previously described subiteration procedures for the aerodynamic and structural methods with a global subiteration strategy. During each subiteration the aerodynamic forces in the structural equations are updated and the new surface displacements are provided to the aerodynamic solver. Using this approach the temporal lag between the aerodynamic and structural equations may be eliminated and a complete synchronization of the aerodynamic/structural equation set is achieved. Any factorization or linearization errors introduced in the equations may also be eliminated using this global subiteration procedure. The resulting coupled procedure retains second-order temporal accuracy.

The importance of synchronizing the aerodynamic and structural equations has been demonstrated in Gordnier and Visbal (2000). In that reference, a long-time numerical instability is shown when no subiterations are used. In this case the structures equations are lagged by one time step. The resulting spurious behavior of this nonsynchronized approach is believed to be attributable to the lagging error in the aerodynamic/structural coupling. This instability is eliminated quite effectively through the use of subiterations.

5. Boundary conditions

The aerodynamic boundary conditions for the delta wing are as follows. On the wing, conditions enforcing flow tangency to the moving surface are applied. The pressure is obtained from the expression $\partial p/\partial n = -\rho \vec{a}_b \cdot \vec{n}$ where $\vec{a}_b$ is the acceleration of the body and $\vec{n}$ is a vector normal to the surface. The density on the surface is determined by extrapolation from interior points. Symmetry is assumed at the wing centerline. At the outflow boundary all variables are extrapolated from the interior using a first-order extrapolation. Quasi-1-D characteristic boundary condition are applied at all other far-field boundaries.

For the delta-wing structural model, clamped boundary conditions are prescribed along the root chord of the delta wing. Free-edge boundary conditions are specified along the leading and trailing edge.

6. Delta wing model

The delta wing geometry considered in the present computations, Fig. 1, corresponds to the half-span delta wing model investigated by Gray et al. (2003). The model consists of a thin-plate aluminum delta wing with a leading-edge sweep angle $\Lambda = 60^\circ$, a root chord length of $c = 450$ mm, and a thickness $\bar{h} = 2$ mm. The structural properties of the aluminum wing are $\rho_s = 2768.65\ \mathrm{kg/m^3}$, $E_s = 6.8944 \times 10^{10}\ \mathrm{N/m^2}$ and $\nu = 0.25$. The wing is assumed to be rigidly clamped along the root chord.

As an initial assessment of the structural model the linear mode shapes and frequencies were computed for the delta wing. Table 1 gives the computed modal frequencies for the first five modes for meshes of 8 × 8, 16 × 16 and 24 × 24 equally distributed elements. The maximum difference in the computed frequencies on the three meshes is on the order of 2% for the first mode. The experimentally measured frequencies (Gray et al., 2003) are also given in Table 1 for the first three modes. Also shown are frequencies computed by Gray et al. (2003) using the ANSYS finite-element package. The modal frequencies from the present structural model are in good agreement with the computed values of Gray et al. but are slightly higher than the experimentally measured values by a maximum of 6.8% in the second mode. Fig. 2 shows the first three computed mode shapes for the half-wing model. The first mode is primarily a bending mode with the maximum deflection at the wing tip. The second mode exhibits more of a torsion-like behavior.

7. Results

Computations are performed with flow conditions corresponding to those in the experimental investigation of Gray et al. (2003), $U_\infty = 30$ m/s, and $\rho_\infty = 1.23\ \mathrm{kg/m^3}$. These conditions result in mass ratio, $\mu_s = 0.1$ and a

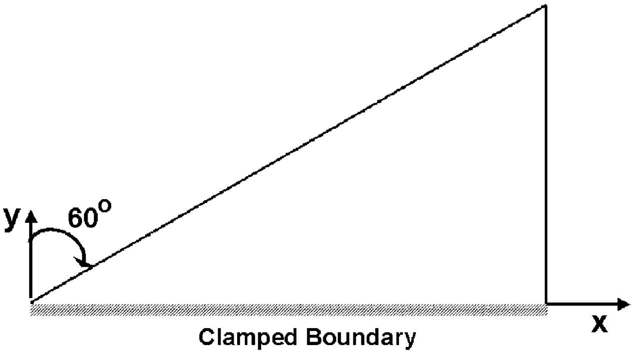

Fig. 1. Delta wing geometry.

Table 1
Computed and experimental linear modal frequencies

Mode	Frequency (Hz)				
	8 × 8	16 × 16	24 × 24	Computed (Gray et al., 2003)	Experimental (Gray et al., 2003)
1	39.95	40.09	39.37	40.67	38.3
2	118.28	118.32	117.69	119.59	110.2
3	206.32	206.22	205.99	209.71	194.1
4	246.10	245.88	245.52		
5	392.18	391.19	391.00		

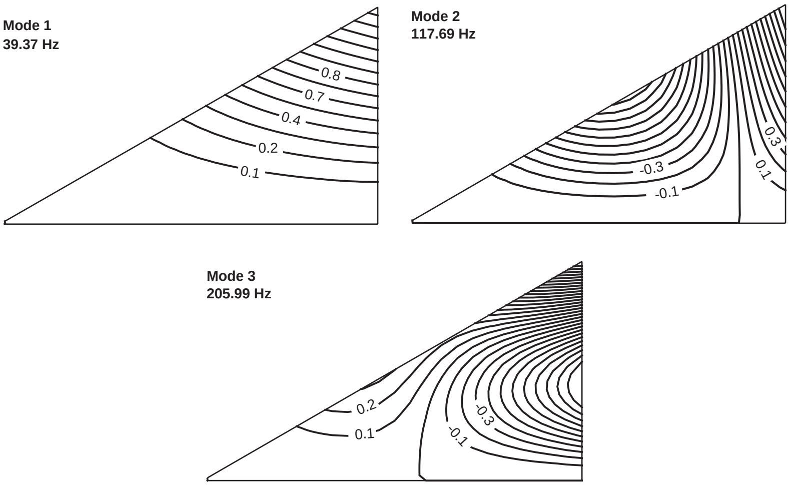

Fig. 2. First three delta wing mode shapes.

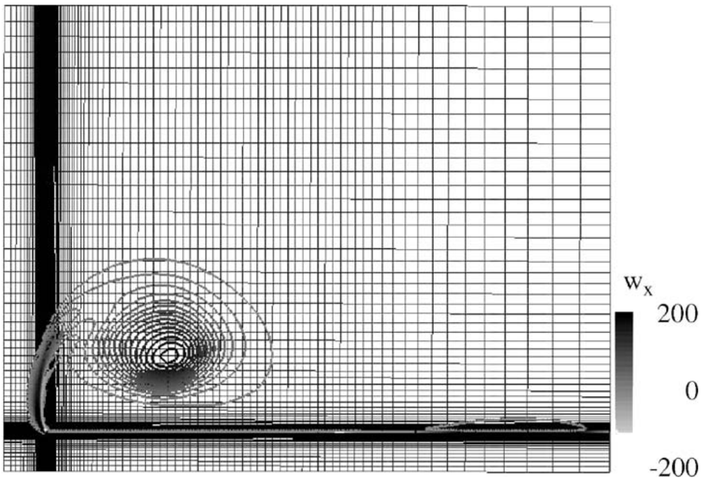

Fig. 3. Mesh resolution for vortical flow: $x/c = 0.5$, $\alpha = 15°$.

nondimensional freestream dynamic pressure $\lambda = 2.0575$. Angles of attack $\alpha = 5°, 15°, 22.5°, 27.5°, 35°$ and $40°$ were simulated.

For the initial computations presented in this work an H–H grid was developed around the delta wing which consists of 141 points in the streamwise direction, 125 points in the spanwise direction and 141 points in the body normal direction. On the delta wing there are 81 equally spaced points in the axial and spanwise direction. In the body normal direction 81 points are located above and 61 points are located below the wing. The axial spacing on the wing is $\Delta x = 0.0125$. The spanwise and body normal mesh points were distributed to provide enhanced resolution in the vortical flow region. Fig. 3 shows a portion of the mesh at an axial location $x/c = 0.5$. The vortex at this location is visualized with contours of axial vorticity to demonstrate the grid resolution being achieved. The surface mesh distribution on the wing for the aerodynamic solver is also used for the finite element model providing a one to one matching between the aerodynamic and structural grids. A nondimensional time step $\Delta\tau = 0.0005$ is employed for all the computations. This time step is chosen based on previous simulations of vortex breakdown (Visbal, 1996) that investigated the influence of time step on the computed unsteady vortex structure.

To initiate the aeroelastic computations, solutions are first obtained for a rigid delta wing. For the angles of attack considered, the resulting flowfields can be classified in three regimes which are illustrated in Fig. 4 by plotting an

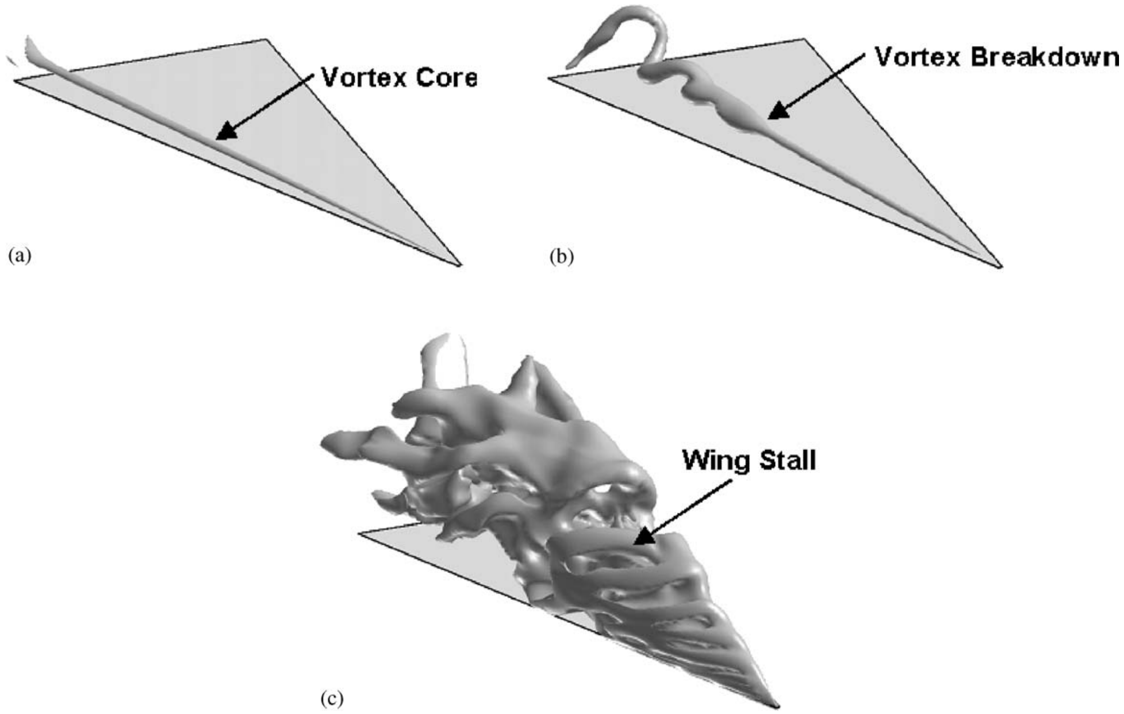

Fig. 4. Types of flow regimes observed: (a) $\alpha = 5°$, (b) $\alpha = 15°$ and (c) $\alpha = 40°$.

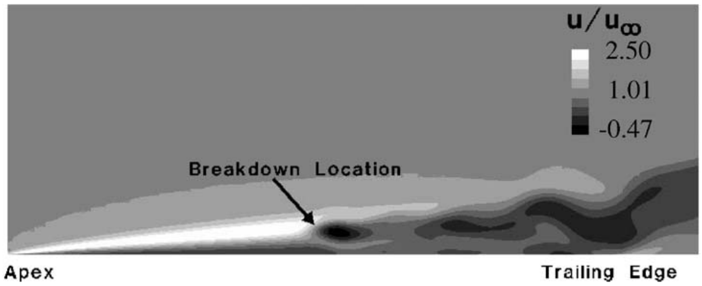

Fig. 5. Axial velocity contours on a plane along the vortex core showing the vortex breakdown location for $\alpha = 15°$.

isosurface of total pressure. At the lowest angle of attack, $\alpha = 5°$, a steady vortex exists over the delta wing for the present Euler simulations. In Fig. 4(a) the vortex core can be seen above the wing surface as a long thin tube. As the angle of attack of the delta wing is increased to $\alpha = 15°$, 22.5°, and 27.5°, this steady vortex structure breaks down, and the familiar spiral vortex breakdown structure advances over the wing. An extensive description of the mean and unsteady structure of spiral vortex breakdown for a 75° sweep delta wing has been given in previous works by Visbal (1995a, b, 1996) and Rockwell (Rockwell, 1993; Ozgoren et al., 2002). As in the present 60° case, the breakdown structure consists of a spiral winding opposite to the vortex swirl which rotates in the swirl direction (as in Fig. 4(b)). Interior to the spiral is a region of reverse axial flow which gives the characteristic switch from jet-like to wake-like flow from upstream to downstream of breakdown. The location of vortex breakdown, therefore, can be defined in a very straightforward manner as the point of maximum upstream penetration of the reversed axial flow, as seen in Fig. 5 for the $\alpha = 15°$ case. This rotating spiral structure produces a significant unsteady pressure signature on the wing surface. The $\alpha = 35°$ case is a transitional point with the vortex approaching the apex of the wing. At this point the flow structure is changing from a vortex breakdown character to a fully stalled flow. For the highest angle of attack, $\alpha = 40°$, a fully stalled flow is observed over the delta wing, Fig. 4(c).

To assess how well the present computations are reproducing the onset and propagation of vortex breakdown over the delta wing, Fig. 6 compares the computed breakdown location with experimental measurements of several investigators (Wentz and Kohlman, 1971; Wolffelt, 1987; Thompson, 1975; Earnshaw and Lawford, 1961). For this comparison the instantaneous breakdown location at the time step used to initialize the aeroelastic computation is employed. This provides a reasonable comparison of the breakdown location though it is known (Menke et al., 1996; Gursul and Yang, 1995) that fluctuations over a limited distance in the axial direction occur at frequencies on the order of St = 0.1. This type of motion of the vortex breakdown location is also observed in the present computations. Computed breakdown points fall within the range of experimentally determined locations with particularly good agreement obtained between the experiments of Wolffelt (1987) and the present simulations.

Each rigid wing solution is advanced 10 characteristic times to establish the initial condition for the aeroelastic computations. The delta wing is then released and allowed to react to the unsteady flowfield over the wing. The level of structural damping is increased during the first several cycles of the response in order to more rapidly damp out the transients resulting from the initial conditions employed. Fig. 7 shows a typical time history of the wingtip deflection for $\alpha = 27.5°$. This wingtip motion can be viewed as a mean deflection with an unsteady fluctuation about the mean value.

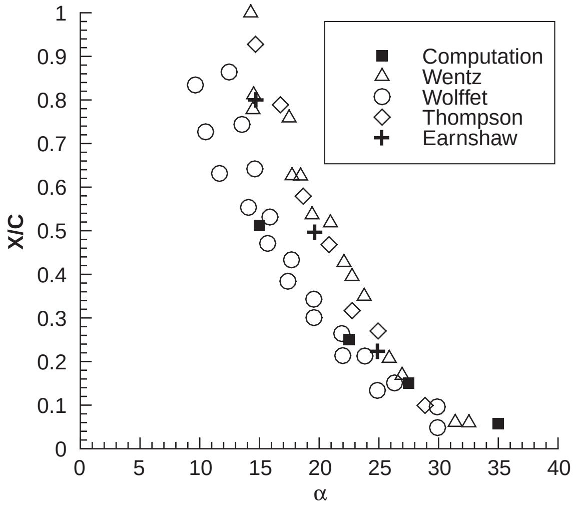

Fig. 6. Comparison of breakdown location with experimental measurements.

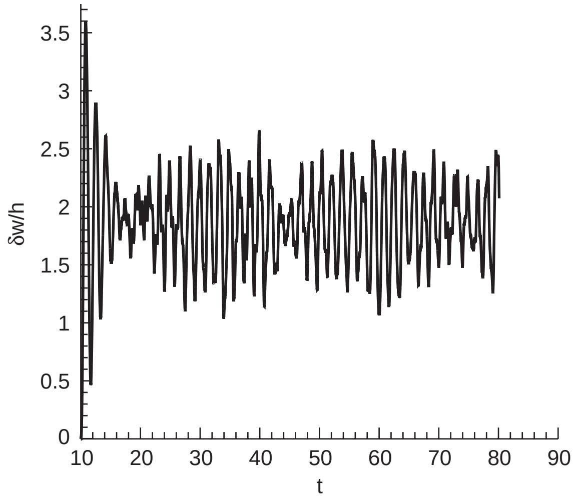

Fig. 7. Time history of the wingtip deflection, $\alpha = 27.5°$.

Fig. 8 plots the mean deformation of the wing for this case. The mean deflection of the wing is primarily a first mode bending at this angle of attack. This result holds true for the other angles of attack not being shown here. Fig. 9 demonstrates how the mean wingtip deflection varies as a function of angle of attack. The mean deflection continually rises as angle of attack is increased up to $\alpha = 35^\circ$. At $\alpha = 40^\circ$ a drop in the mean deflection occurs. This decrease in the deflection results from the loss of the additional suction from the vortical flow with the onset of a fully stalled flow over the delta wing for $\alpha \geqslant 35^\circ$.

To investigate the buffeting response of the delta wing the rms acceleration at the wing tip is plotted as a function of angle of attack in Fig. 10 and compared with the experimental measurements of Gray et al. (2003). Good qualitative

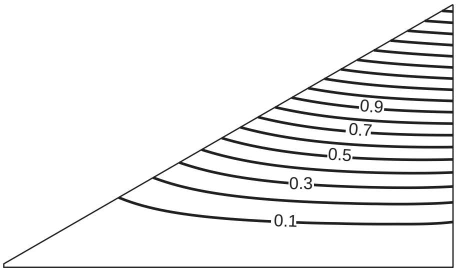

Fig. 8. Mean deflection ($\delta w/h$) of the delta wing at $\alpha = 27.5^\circ$.

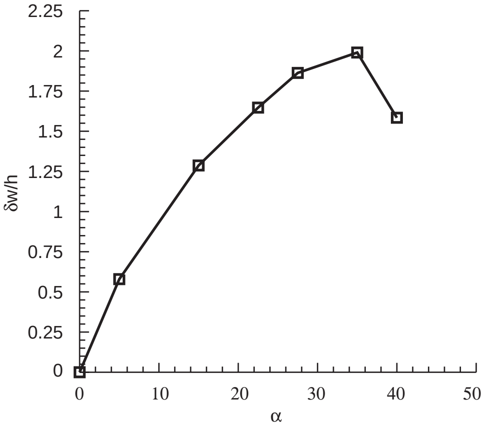

Fig. 9. Mean wingtip deflection as a function of angle of attack.

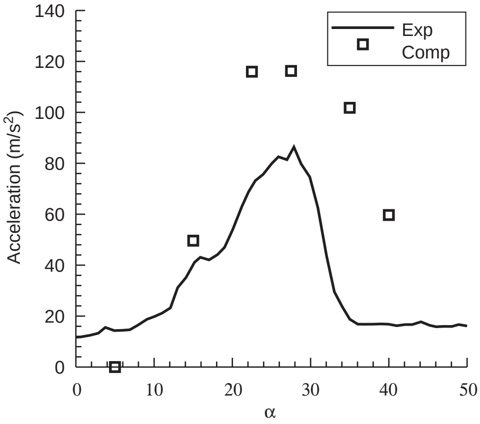

Fig. 10. The r.m.s. of wingtip acceleration as a function of angle of attack.

agreement is seen between the experimental response and the computational points. As suggested by Gray et al. (2003), a rapid increase in the buffet response of the wing occurs as vortex breakdown moves over the wing between $\alpha = 5^\circ$ and 22.5° (see Fig. 6). As the breakdown approaches the apex the r.m.s. acceleration reaches its maximum values for $\alpha = 22.5^\circ - 27.5^\circ$. In this region the maximum computational accelerations exceed the experimental values by approximately 32.5% and the computations show a somewhat broader peak region than the experiments. As the vortex breakdown reaches the apex of the wing and the onset of wing stall occurs, $\alpha = 27.5^\circ - 40^\circ$, the level of buffeting rapidly reduces as seen in the experiments.

A number of factors may contribute to the discrepancy between the peak acceleration values. Experimentally, there are uncertainties associated with the level of structural damping and wind tunnel wall influences. In the computations, no secondary vortex is produced in the Euler simulations. Therefore, the primary vortex is located further outboard on the wing. This will effectively enhance the influence of the vortical flow on the structural response, leading to higher levels of fluctuations. Given these uncertainties the difference in peak acceleration between the computations and the experiment does not seem unreasonable. At an angle of attack $\alpha = 5^\circ$, a steady response is computed while the experiments exhibit a low level of buffeting. This difference between the computation and experiment may arise from unsteady viscous effects not captured in the present inviscid Euler computations.

Spectral analysis of the wingtip motion at various angles of attack, Fig. 11, exhibits a dominant peak at St = 0.606 or 40.4 Hz. This corresponds to the frequency of the first structural mode of the delta wing. Somewhat smaller peaks are observed at the frequencies of the second and third structural modes, St = 1.755 (117 Hz) and St = 3.089 (205.9 Hz) indicating higher mode participation. At the highest angle of attack, $\alpha = 40^\circ$, these peaks at the higher mode frequencies are no longer observed for the wingtip deflection, Fig. 11(d).

Spectral analysis of the wingtip acceleration is also carried out for the same angles of attack, Fig. 12. These results show significant peaks at frequencies corresponding to the first three structural modes (40, 117 and 206 Hz) and indicate more strongly the participation of the second and third structural modes for angles of attack where breakdown is on the wing. These observations are consistent with the experimental spectral analysis of Gray et al. (2003) which showed spectral peaks at the first three experimental modal frequencies (38, 110 and 194 Hz). The slightly higher frequencies in the computation are due to the differences between the computed and measured modal frequencies for the delta wing, Table 1. In the experiment most of the energy is in the second and third modes. This is also true in the computations although more participation of the first mode is observed than in the experiments of Gray et al. (2003). At $\alpha = 40^\circ$,

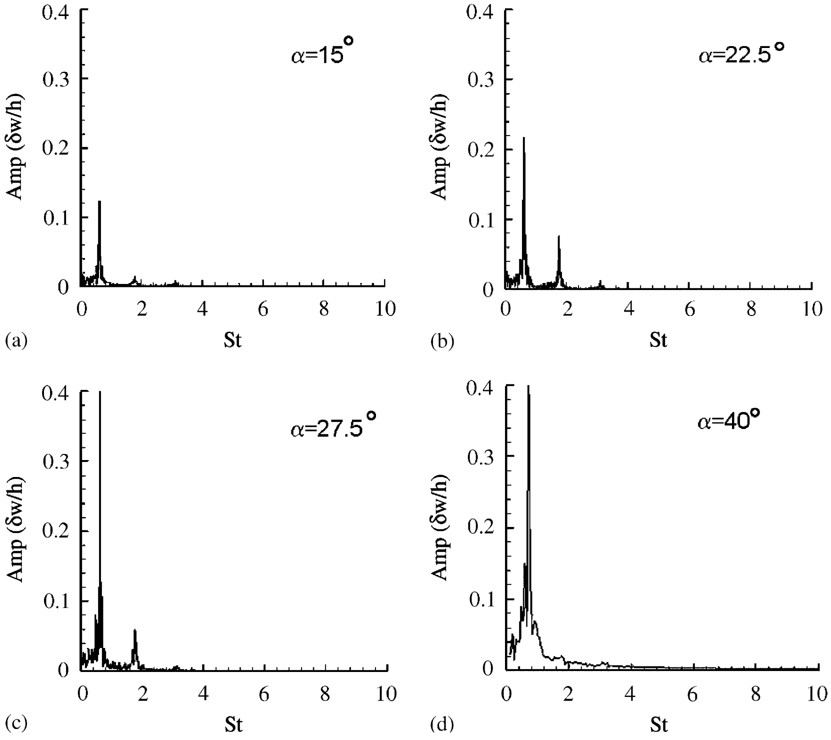

Fig. 11. Spectral analysis of wingtip deflection for various angles of attack.

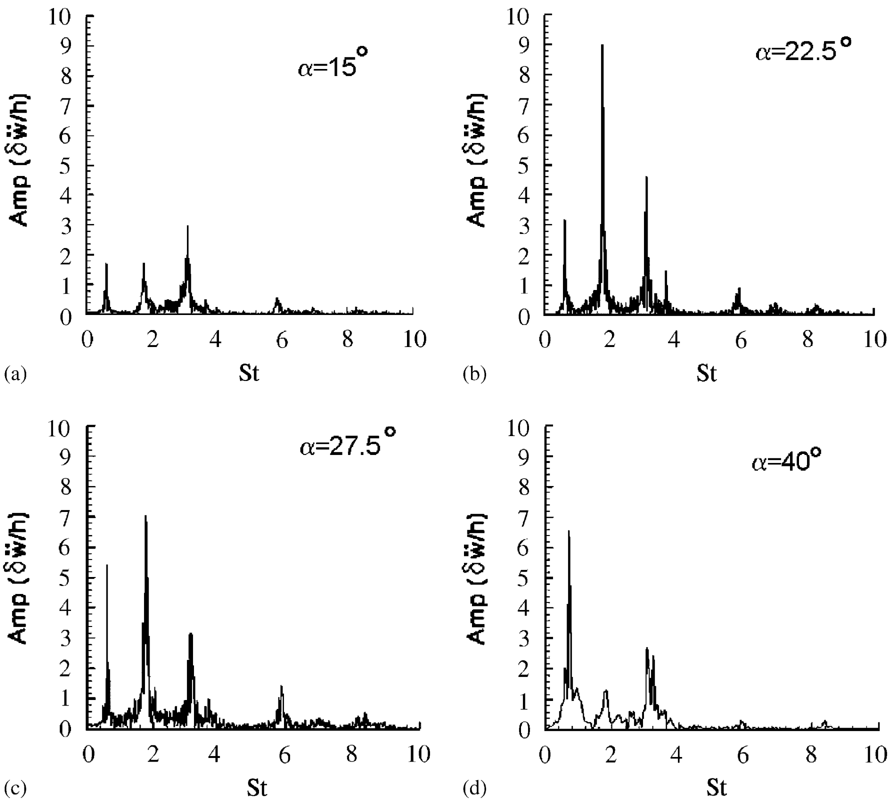

Fig. 12. Spectral analysis of wingtip acceleration for various angles of attack.

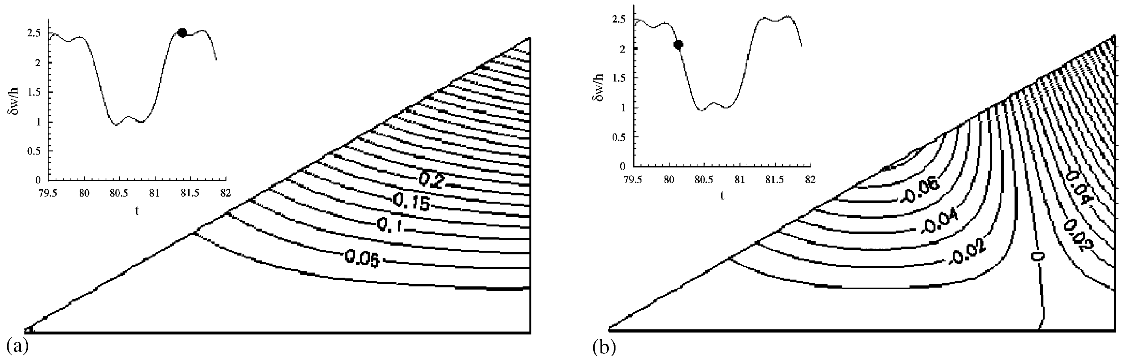

Fig. 13. Contours of $\Delta\delta w/h$ at two different instants of the wingtip response cycle for $\alpha = 27.5°$.

when the wing is fully stalled, the peaks for the higher modes are significantly reduced as compared to the first mode peak.

Due to the dominance of the first structural mode in the delta wing response, it is difficult to observe the higher mode participation detected in the spectral analysis from plots of the wing deflection alone. If the effect of the mean deflection is removed, however, by plotting the difference between the instantaneous and mean deflection, the higher mode influence can be more easily discerned. Fig. 13 plots contours of $\Delta\delta w/h = (\delta w/h)_{\text{inst}} - (\delta w/h)_{\text{mean}}$ at two different instants during a cycle of the wingtip deflection for the $\alpha = 27.5°$ case. At a point of maximum deflection, Fig. 13(a), the contours of $\Delta\delta w/h$ exhibit the dominant first mode character of the deflection. In Fig. 13(b), however, where the wingtip has a downward motion, the influence of the higher mode is seen with the contours of $\Delta\delta w/h$ showing the character of the second mode.

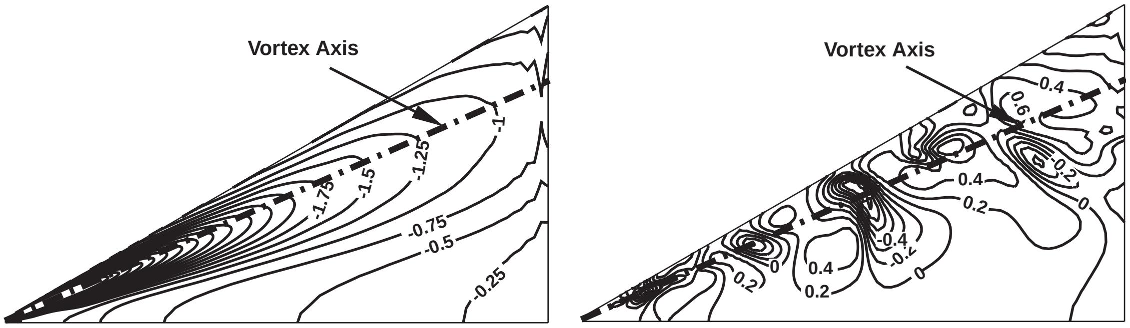

(a) (b)

Fig. 14. Surface pressure coefficient on the upper surface of the delta wing for $\alpha = 27.5^\circ$: (a) mean value (b) instantaneous perturbation from the mean, ΔCp.

To further explore how the spiral vortex breakdown gives rise to the buffeting of the delta wing, the unsteady surface pressure for the $\alpha = 27.5^\circ$ case is examined. For this angle of attack, vortex breakdown is located at approximately $x/c = 0.15$. As with the deflection, the surface pressure can be represented as a mean pressure and an instantaneous perturbation from the mean. Contours of the mean pressure coefficient on the upper surface of the delta wing are shown in Fig. 14(a). An area of low pressure is located outboard towards the leading edge of the wing underneath the vortex. This area of low pressure produces the mean upward deflection of the wing seen in Fig. 8. Fig. 14(b) displays contours of the instantaneous pressure difference $\Delta Cp = Cp_{\text{inst}} - Cp_{\text{mean}}$. Alternating regions of positive and negative pressure differentials are seen. The regions of lower pressure correspond to locations where the spiral structure associated with the vortex breakdown is near the surface of the wing. As this spiral structure rotates, these regions of low pressure propagate downstream producing the pressure fluctuations that excite the wing buffeting. The largest pressure differential for this case occur around the midpoint of the delta wing.

To better understand these unsteady pressure fluctuations, Fig. 15 shows the results of a spectral analysis of the surface pressure at four axial locations located underneath the vortex core. The peak amplitudes are seen at the axial location $x/c = 0.5$ and are characterized by a broadband frequency range from $\text{St} = 1.6$ to $\text{St} = 3.6$ with the maximum amplitude at a frequency $\text{St} = 2.14$. The pressure fluctuations at this location result from the strong interaction of the unsteady spiral structure of vortex breakdown with the wing surface as described previously, Fig. 14(b). At locations further downstream this peak in the spectral response diminishes as the spiral nature of the vortex breakdown becomes less coherent. These broadband pressure fluctuations are responsible for exciting the buffet response of the first three modes of the delta wing. In particular, the frequencies of the second and third modes lie directly in the broadband frequency range of the pressure fluctuations giving rise to the additional second and third mode response observed for the delta wing. Clearly, the location on the wing where the spiral associated with the breakdown interacts most significantly with the wing surface will be a key factor in determining the resulting level of wing buffeting.

8. Conclusions

The buffeting response of a 60° sweep delta wing resulting from pressure fluctuations associated with vortex breakdown has been investigated numerically. An aeroelastic code which couples an Euler solver with a finite element model for the von Karman plate equations is used for these computations. Implicit coupling of the aerodynamic and structural solvers is achieved via a subiteration strategy and the resulting scheme is second order accurate in time. Comparisons of the computed linear modal frequencies and the mode shapes of the delta wing showed good agreement with experimentally determined values and other finite element simulations.

Computations for the flexible delta wing were performed for a range of angles of attack, $\alpha = 5^\circ - 40^\circ$. The resulting flowfields over the wing can be categorized into three regimes: steady vortical flow, vortex breakdown on the wing and fully stalled flow. For low angles of attack before vortex breakdown occurs on the wing, no buffeting of the wing is observed for these simulations using the Euler equations. As vortex breakdown moves onto the wing a rapid increase in the buffeting response occurs due to the unsteady pressure fluctuations associated with the spiral vortex breakdown. As the breakdown reaches the apex and the wing stalls, the buffeting response decreases. This trend is consistent with previous experimental observations.

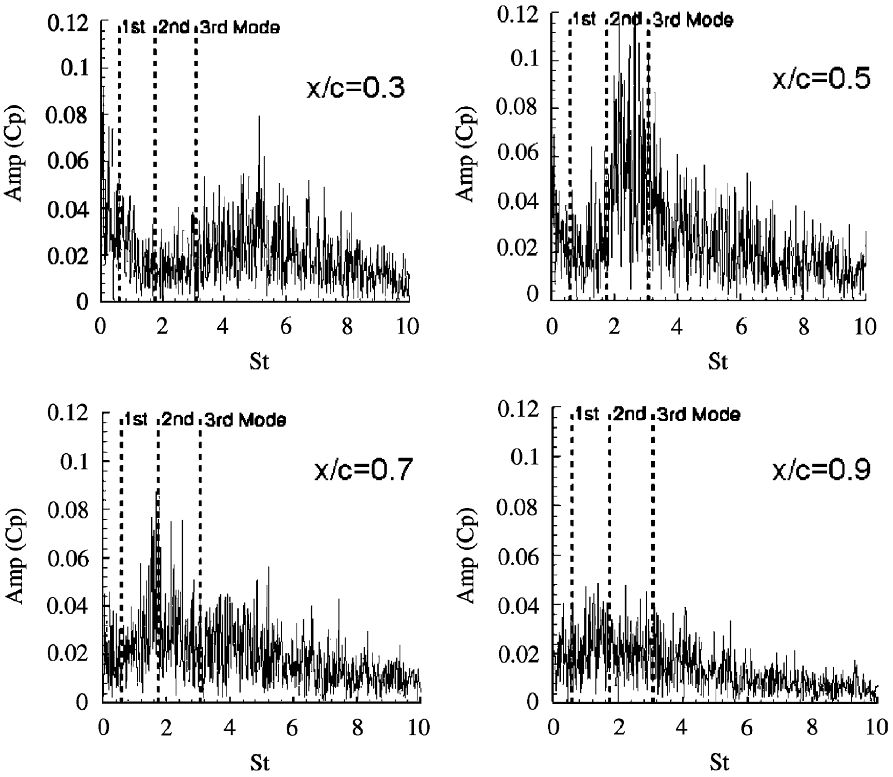

Fig. 15. Spectral analysis of pressure fluctuations under the vortex core for $\alpha = 27.5°$.

Comparisons of the computed r.m.s. acceleration of the wing tip with experimental measurements showed good qualitative agreement and reasonable quantitative agreement given the experimental uncertainties and the inviscid aerodynamic modelling used. Spectral analysis of the wingtip deflections showed the first structural mode to be the dominant mode. As in the experiment, the spectral analysis of the wingtip acceleration indicated more clearly contributions also from the second and third structural modes.

Acknowledgements

This work was produced with AFOSR sponsorship under task 2304IW monitored by Maj. W. Hilbun and Dr T. Beutner. The authors would like to thank Dr Ismet Gursul for several valuable discussions about his experimental results. This work was supported in part by a grant of HPC time from the DoD HPC Shared Resource Centers at the Naval Oceanographic Office.

References

Beam, R.M., Warming, R.F., April 1978. An implicit factored scheme for the compressible Navier–Stokes equations. AIAA Journal 16, 393–402.

Chia, C., 1980. Nonlinear Analysis of Plates. McGraw-Hill International Book Company, New York.

Earnshaw, P.B., Lawford, J.A., 1961. Low-speed wind-tunnel experiments on a series of sharp-edged delta wings, pt 1. Royal Aircraft Establishment RAE TN Aero 2780.

Gaitonde, D., Edwards, J., Shang, J., 1995. The computed structure of a 3-D turbulent interaction caused by a cylinder/offset flare juncture. AIAA Paper 95-0230.

Gordnier, R.E., April 2002. Computation of limit-cycle oscillations of a delta wing. AIAA-2002-1411.

Gordnier, R.E., Fithen, R., June 2001. Coupling of a nonlinear finite element structural method with a Navier–Stokes solver. AIAA-2001-2853.

Gordnier, R.E., Visbal, M.R., June 1991. Numerical simulation of the unsteady vortex structure over a delta wing. AIAA-91-1811.

Gordnier, R.E., Visbal, M.R., January–February 1994. Unsteady vortex structure over a delta wing. Journal of Aircraft 31, 243–248.

Gordnier, R.E., Visbal, M.R., June 2000. Development of a three-dimensional viscous aeroelastic solver for nonlinear panel flutter. AIAA 2000-2337.

Gray, J.M., Gursul, I., Butler, R., January 2003. Aeroelastic response of a flexible delta wing due to unsteady vortex flows. AIAA-2003-1106.

Gursul, I., Xie, W., 1999. Buffeting flows over delta wings. AIAA Journal 37, 58–65.

Gursul, I., Yang, H., 1995. On fluctuations of vortex breakdown location. Physics of Fluids 1, 229.

Humar, J.L., 1990. Dynamics of Structures. Prentice-Hall, Englewood Cliffs, NJ.

Jameson, A., Schmidt, W., Turkel, E., 1981. Numerical solutions of the Euler equations by finite volume methods using Runge–Kutta time-stepping schemes. AIAA-81-1259.

Melville, R.B., Morton, S.A., Rizzetta, D.P., June 1997. Implementation of a fully-implicit, aeroelastic Navier–Stokes solver. AIAA 97-2039.

Menke, M., Yang, H., Gursul, I., January 1996. Further experiments on fluctuations of vortex breakdown location. AIAA-96-0205.

Morton, S.A., Melville, R.B., Visbal, M.R., April 1997. Accuracy and coupling issues of aeroelastic Navier–Stokes solutions on deforming meshes. AIAA 97-1085.

Ozgoren, M., Sahin, B., Rockwell, D., 2002. Vortex structure on a delta wing at high angle of attack. AIAA Journal 40, 285–292.

Pulliam, T.H., Chaussee, D.S., February 1981. A diagonal form of an implicit approximate-factorization algorithm. Journal of Computational Physics 39, 347–363.

Pulliam, T.H., Steger, J.L., February 1980. Implicit finite-difference simulation of three-dimensional compressible flows. AIAA Journal 18, 159–167.

Reddy, J.N., 1993. An Introduction to the Finite Element Method. McGraw-Hill, New York.

Rockwell, D., January 1993. Three-dimensional flow structure on delta wings at high angle-of-attack: experimental concepts and issues. AIAA-93-0550.

Tang, D., Dowell, E.H., 2001. Effects of angle of attack on nonlinear flutter of a delta wing. AIAA Journal 39, 15–21.

Tang, D., Henry, J.K., Dowell, E.H., 1999. Limit cycle oscillations of delta wing models in low subsonic flow. AIAA Journal 37, 1355–1362.

Tang, D., Henry, J.K., Dowell, E.H., 2001. Nonlinear aeroelastic response of delta wing to periodic gust. Journal of Aircraft 37, 155–164.

Tang, D., Henry, J.K., Dowell, E.H., 2002. Effects of steady angle of attack on nonlinear gust response of a delta wing model. Journal of Fluids and Structures 16, 1093–1110.

Thompson, D.H., 1975. A water tunnel study of vortex breakdown over wings with highly swept leading edges. Australian Research Labs, Note ARL/A356.

Visbal, M.R. January, 1995a. Computational and physical aspects of vortex breakdown on delta wings. AIAA-95-0585.

Visbal, M.R. June, 1995b. Numerical simulation of spiral vortex breakdown above a delta wing. AIAA-95-2309.

Visbal, M.R. June, 1996. Computed unsteady structure of spiral vortex breakdown on delta wings. AIAA-96-2074.

Wentz, W.H., Kohlman, D.L., 1971. Vortex breakdown on slender sharp-edged wings. Journal of Aircraft 8, 156–161.

Wolffelt, K.W., 1987. Investigation on the movement of vortex burst position with dynamically changing angle of attack for a schematic delta wing in a water channel with correlation to similar studies in wind tunnel. In: Aerodynamic and Related Hydrodynamic Studies Using Water Facilities. AGARD-CP-413.